Heliyon 9 (2023) e18780

Contents lists available at ScienceDirect

Heliyon

journal homepage: www.cell.com/heliyon

Electronic, electrical and thermoelectric properties of $Ba_{0.95}Ca_{0.05}Ti_{0.95}Y_{0.05}O_{2.975}$ compound: Experimental study and DFT-mBJ calculation

A. Saidi [a,*], A. Mabrouki [a], R. Dhahri [a], E. Dhahri [a], K. Khirouni [b], B.F.O. Costa [c]

[a] Laboratoire de Physique Appliquée, Faculté des Sciences, Université de Sfax, Tunisia
[b] Laboratoire de Physique des Matériaux et des Nanomatériaux Appliquée à l'Environnement, Faculté des Sciences, Université de Gabes, Tunisia
[c] University of Coimbra, CFisUC, Physics Department, P-3004-516 Coimbra, Portugal

ARTICLE INFO

Keywords:
TB-mBJ calculation
Solid-state method
Impedance spectroscopy
Real permittivity
Dielectric behavior

ABSTRACT

This article explores the impact of co-doping $BaTiO_3$ ceramics with Ca^{2+} and Y^{3+} using solid-state reactions to improve its dielectric constant and decrease losses. The oxide BCTYO ($Ba_{0.95}Ca_{0.05}Ti_{0.95}Y_{0.05}O_{2.975}$) exhibits a tetragonal crystal structure, characterized by a space group of *P4mm*. By examining the behavior of the doped $BaTiO_3$ sample and performing simulations, researchers can better understand the underlying mechanisms and optimize material properties for specific applications. DFT study shows a semiconductor behavior with an indirect gap ($E_g = 2.5$ eV). The partial DOS proves that the hybridization between the orbitals Ti 3d, Y 3d, and O 2p is responsible for the band gap and the hopping processes. The analysis of conductivity curves provides evidence for the semiconductor characteristics of the material under investigation. By determining the activation energy (E_a) through analyzing Ln(f_{max}) and conductivity as a function of 1000/T, the interconnection between conduction and relaxation phenomena is demonstrated. The study of the real part of the dielectric permittivity (ε') shows a transition at $T_c = 380$ K. The obtained results are promising and indicate that the studied material has the potential for various electronic applications (energy storage and diode fabrication …). Moreover, the thermal, electrical, and thermoelectric characteristics were examined utilizing the semi-classical Boltzmann theory. The findings revealed an intriguing result, suggesting that $Ba_{0.95}Ca_{0.05}Ti_{0.95}Y_{0.05}O_{2.975}$ holds promise as a potential candidate for application in thermoelectric devices.

1. Introduction

Recently, there has been significant research on perovskite multiferroic materials, specifically $BaTiO_3$(barium titanate), and their derivatives, due to their wide range of applications [1–4]. The high dielectric constant, ferroelectric behavior, spontaneous polarization, and nonlinear optical coefficients of $BaTiO_3$ have captured significant interest [5,6]. It finds widespread application in a variety of uses, including multilayer ceramic capacitors, thermometers, infrared detectors, and bolometers [7,8]. However, it has limitations like a high loss tangent and limited operating temperature range. To overcome these limitations, researchers have explored modifications of $BaTiO_3$ by doping and substitution techniques. One such modification involves the addition of Ca (calcium) to $BaTiO_3$, resulting in $Ba_{1-x}Ca_xTiO_3$ ($BCTO_3$). Ca-doped $BaTiO_3$ exhibits low dielectric loss and remains unaffected by temperature, making it a

* Corresponding author.
E-mail address: amirasaidipc3@gmail.com (A. Saidi).

https://doi.org/10.1016/j.heliyon.2023.e18780
Received 15 May 2023; Received in revised form 25 July 2023; Accepted 27 July 2023
Available online 29 July 2023

promising candidate for lead-free electro-optical modulators and memory devices [9,10]. The tetragonal ferroelectric phase stabilization in $BCTO_3$ is achieved by substituting Ca for Ba in the $BaTiO_3$ structure [11,12]. This doping technique improves the transport properties of BTO compounds, including the Curie temperature (T_c) [13,14]. At room temperature, $Ba_{0.83}Ca_{0.17}TiO_3$ adopts a tetragonal crystalline structure, characterized by the space group *P4mm* [15]. Among the materials synthesized with different x values (0.10, 0.15, 0.20, and 0.25) using the hydrothermal technique, $Ba_{0.80}Ca_{0.20}TiO_3$ demonstrates favorable results, with a transition temperature (T_c) of 135 K and a dielectric permittivity (ϵ_r) of approximately 4548 [16]. Furthermore, Rashwan et al. synthesized the compound ($Ba_{0.95}Ca_{0.05}$) TiO_3 using the solid-solid process and found that it exhibits the highest values of maximum permittivity (ε_{max}), reaching 1982. On the other hand, many studies prove that the presence of oxygen vacancy enhances the electric, optical, and the material's gas detection properties [17]. Tehtih et al. found that the insertion of Y ions decreases the band gap [18]. Other researchers are focused on clarifying the optical properties of the materials using the spectral element method [19–22]. Currently, we find ourselves in an era known as the energy accumulation era, where the world faces two interconnected challenges: ensuring a stable supply of primary energy and embracing renewable and eco-friendly sources. Researchers are especially intrigued by a significant and difficult task that entails effectively collecting waste heat and transforming it into electrical energy using economical and ecologically responsible approaches. Thermoelectric materials play a crucial role in addressing this challenge by enabling the direct conversion of heat into electricity. The merit factor, denoted as ZT, ($S^2\sigma/k$) T, serves as a valuable parameter for evaluating the effectiveness of a material in thermoelectric applications. To enhance the properties of these materials, researchers are actively working on lowering heat conductivity [23]. Various approaches, such as incorporating nanostructures or introducing layered structures, are being explored as potential solutions. Oxide semiconductor materials, including perovskite, show great potential as a promising option for high-temperature thermoelectric applications due to their excellent thermal and chemical stability [24]. Notably, significant progress has been made in achieving impressive thermoelectric performance in various oxide materials, such as p-type NaxCoO2 [25], $Ca_3Co_4O_9$ [26], BiCuSeO [27], and n-type $SrTiO_3$ [28], ZnO [29], and Sr2BBO6 oxides [30]. T his research paper extensively

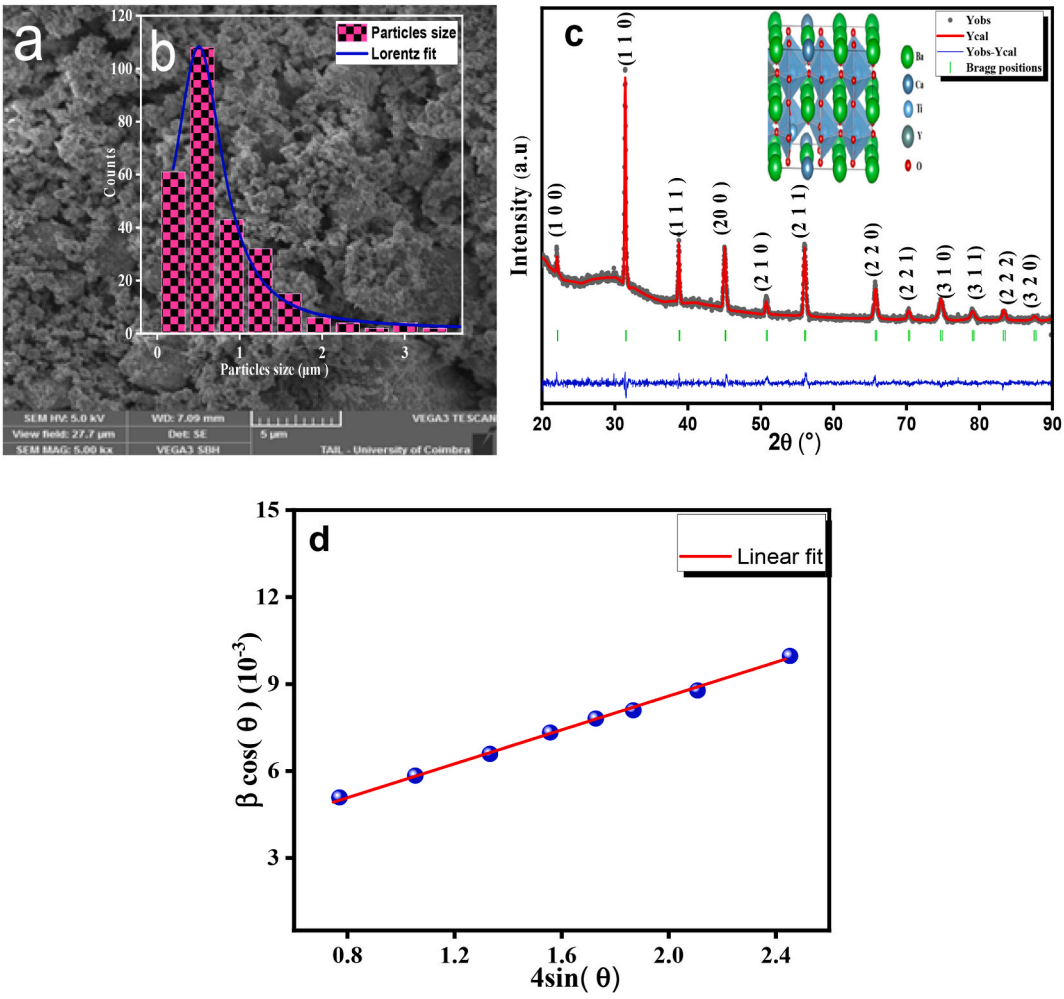

Fig. 1. (a) SEM image; (b) particle size distribution of the perovskite BCTYO; (C) XRD with Rietveld refinement of BCTYO compound; (d) Williamson Hall plot for BaCaTiYO sample.

investigates the effects of co-doping on the structural, transport properties of BCTYO ceramic. The objective of this study is to enhance the electrical characteristics of BTO by altering its composition through the partial substitution of Ca and Y. Notably, a novel approach is adopted as a DFT calculation is carried out for the first time to explore the structural, optical, electronic, and thermoelectric properties of the $Ba_{0.95}Ca_{0.05}Ti_{0.95}Y_{0.05}O_{2.975}$ compound. Our material possesses unique attributes that make it suitable for diverse applications across various fields. These applications include lead-free ceramics, electronic devices, thermoelectric applications, LTTC applications, non-volatile memories, and optical devices with a 2.5 eV energy band.

2. Experimental section

The $Ba_{0.95}Ca_{0.05}Ti_{0.95}Y_{0.05}O_{2.975}$ sample was elaborated by solid-state method, in which high-purity precursors (99.9%) of $BaCO_3$, $CaCO_3$, TiO_2, and Y_2O_3 were weighing with stoichiometric proportions and mixed using an agate mortar. The powder obtained undergoes a cycle of grinding, pelletizing, and sintering for 12 h at different temperatures (800-900- 1100 and 1300). The obtained sample was characterized by X-ray diffraction to ensure its purity, employing a (θ, 2θ) type powder diffractometer using the Kα1 line (λ = 1.5406 Å) of a copper anticathode. The structural parameters were checked by exploiting Rietveld refinement by utilizing FullProf software [31]. The scanning electron microscope used for the micrography of our material is a Zeiss Ultra Plus. The electronic bombardment is carried out using an accelerating voltage that can vary in the range of 0.5–30 kV; the images were taken at 5 kV.

2.1. Computational detail

In order to correctly modulate the $Ba_{0.95}Ca_{0.05}Ti_{0.95}Y_{0.05}O_{2.975}$ compound, we have created a 4 × 2*5 supercell that contains 38 Ba, 2 Ca, 38 Ti, 2 Y, and 119 oxygen atoms. The DFT calculation was performed using the GGA approximation [2,32,33] using the hybrid method with full FP L/APW + lo potential implemented in the Wien2k package [34]. To obtain a band gap value that was closer to that obtained in the experiment, we included the modified Becke−Johnson (DFT- mBJ) potential Tran−Blaha. We used experimental lattice parameters determined by the XRD measurement X-ray extracted from the Rietveld refinement. We have chosen 500 K **points** in the irreducible Brillouin zone. Every structure underwent complete relaxation, ensuring that the residual force on each atom was less than 0.02 eV/Å. Additionally, the total energy was converged to 10^{-4} eV per atom for the calculations.

3. Results and discussions

3.1. Morphological and structural properties

In Fig. 1(a), the SEM image and particle size distribution of the perovskite BCTYO are depicted. The image reveals randomly scattered irregularly shaped agglomerated grains, which contribute positively to enhancing the ceramic's physical properties and density. Fig. 1(b) displays the particle size distribution obtained through the use of ImageJ software. The histogram of the distribution closely follows a Gaussian function, indicating an average particle size of approximately 0.50 μm.

The XRD analysis of the material elaborated by the solid-solid method shows the presence of fine and intense peaks reflecting good crystallization (Fig. 1(c)). The Rietveld refinement using the FullProf software indicates the existence of the primary BCTYO phase, which forms a tetragonal crystal structure with space group *P4mm*, and a secondary phase of low intensity that is attributed to titanium dioxide (TiO_2). The information pertaining to the structural parameters can be found in Table 1.

The Williamson-Hall formula was used to calculate the median dimension of crystallites (D_{WH}), and is represented by Equation **(1)** [35]:

$$\beta \cos(\theta) = \frac{k\lambda}{D} + 4\varepsilon \sin(\theta) \quad (1)$$

Where, β and θ denote is the FWHM and the Bragg angle corresponding to each peak respectively, λ stands for the Cu wavelength, k is a shape factor with a value of 0.9, $D_{W\text{-}H}$ represents the crystallite size, and ε represents a coefficient associated with the strain effect.

The average crystallite's size is estimated from the intercept with the y-axis Fig. 1(d). The average crystallite size measured is about 50 nm. The theoretical density (d_x) of the studied material can be calculated using the following equation **(2)** [36]:

Table 1
The refinement parameters of BCTYO.

Sample and Space Group	Cell parameters	Values
BaCaTiYO *P4mm*	*a (Å)*	4.000(5)
	c (Å)	4.010(4)
	V (Å^3)	64.16(2)
	R_p *(%)*	4.93
	R_{wp} *(%)*	6.40
	R_F *(%)*	5.74
	χ^2 (%)	1.26

$$d_x = \frac{ZM}{Na^2c} \tag{2}$$

Where M is the molar mass, N is the Avogadro number ($6.022.10^{23}$), and ***a*** is the parameter of the cell. The calculation of the density gives a value in the order of 5.083 g. cm^{-3}.

4. Electronic properties

Fig. 2(a) depicts the electronic band structures of $Ba_{0.95}Ca_{0.05}Ti_{0.95}Y_{0.05}O_{2.975}$ sample calculated using TB−mBJ approaches, based on the selected high-symmetry paths [37–40] $\Gamma - X - M - \Gamma - Z - R - A - Z - R - X$ (Fig.2(b)). Like $BaTiO_3$, which has a semi-conductor indirect band ($E_g = 3.2$ eV) [32,33,41]. An S.C behavior was observed with a direct bandgap Eg = 2.5 eV [42] which makes this material significant utility in the production of diodes and photovoltaic panels. This is mainly due to its unique electronic properties, which allow the conversion of sunlight into electrical energy. In order to gain deeper insights into the electronic structure, we examined the density of states for the material under investigation as depicted in Fig. 2(c and d). The comprehensive analysis of both total and partial density of states revealed that the upper portion of the valence band (VBM) primarily originates from a combination of Ti and Y 3d states along with 2p states. On the other hand, the conduction band minimum (CBM) is predominantly occupied by Ti 3d transition-metal states. Notably, Ba and Ca were found to have no significant contribution to either VBM or CBM.

Fig. 2(e) shows how the absorption coefficient changes concerning photon energy. On the bases of the result shown in the Bands Structure and according to the Tauc relation [24,43], we traced in the inset of Fig. 2(e) the evolution of $(\alpha h\nu)^{1/2}$ as function of ($h\nu$) which is given by equation **(3)** :

$$(\alpha h\vartheta)^2 = A(h\vartheta - Eg) \tag{3}$$

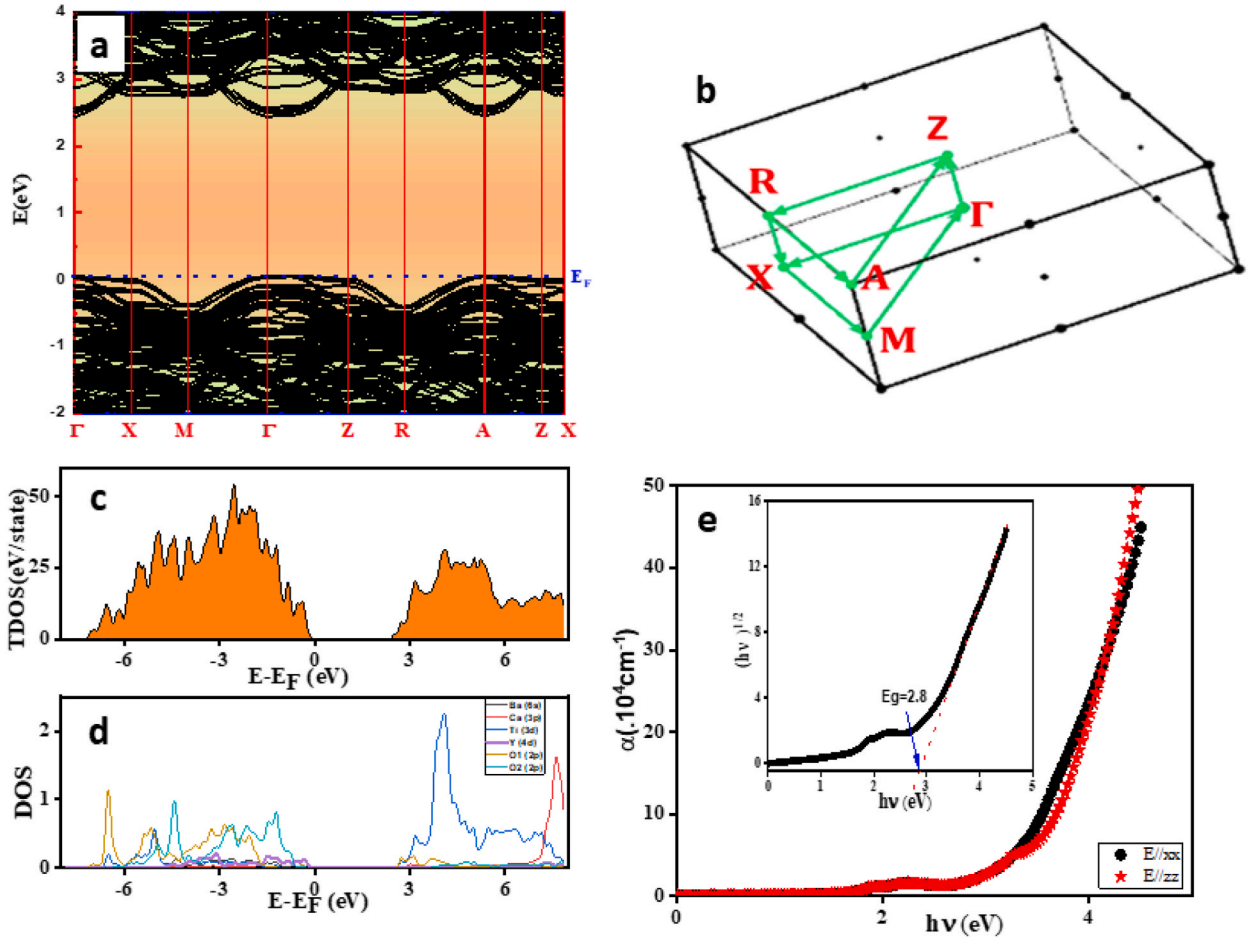

Fig. 2. Illustrates various aspects of BCTYO samples: (a) The band structure; (b) The 3D representation of the bands around the Γ − X − M − Γ −Z − R − A − Z − R − X paths in the Brillouin zone; (c) The total density states; (d) The partial density of states for the BCTYO sample; and (e) The changes in the absorption coefficient as function of the photon energy, with the Tauc plot shown in the inset.

A is a constant and ħϑ is the photon energy. The lack of contrast between the absorption in the two directions shows the absence of anisotropy in the material.

5. Electrical properties

The dependency of (Z′) on frequency at various temperatures is shown in Fig. 3(a), and it shows a considerable decline over a number of decades. This confirms the conduction process's thermal activation, attributed to the rise in conductivity (σ). In the high-frequency range, the values of Z′ converge irrespective of temperature. This outcome can be associated to the liberation of charges due to barrier reduction and the presence of a space charge zone (SCZ) [44].

Fig. 3(b) illustrates the change in Z″ vs. frequency for various temperatures. The peak frequency of Z″ changes towards a greater value as the temperature rises. This discovery provides evidence for the presence of a relaxation phenomenon in the material [45]. Other studies on perovskite-type materials have observed the same behavior [46]. By extracting the maximum frequency from the observed peaks in the impedance spectrum Z'' = f (frequency) at different temperatures, we can determine the activation energy E_a on the basis of Arrhenius law, we use equation (4) [47]:

$$f_{max} = f_0 \exp\left(\frac{-E_a}{k_B.T}\right) \tag{4}$$

With E_a: activation energy and K_B: Boltzmann constant ($K_B = 8.617\ 10^{-5}$ eV K^{-1}), f_0: frequency factor, and T: temperature in kelvin.

The formula mentioned in your statement describes the variation of the logarithm of the frequency, Ln (f_{max}), vs. 1000/T. This relationship was observed in Fig. 3(c), which shows a linear behavior for the data points. This linear behavior demonstrates that the examined material's conduction mechanism is thermally activated. The estimated value of the activation energy is $E_a = 1.38$ eV.

At varying temperatures, the Nyquist plot of the BCTYO displays the existence of one semicircle per temperature, as illustrated in Fig. 4(a). This means that the electrode-material interface doesn't contribute to the electrical response; the presence of a single semicircle indicates that the electrical conduction of the samples is governed by a single primary mechanism. The equivalent electrical

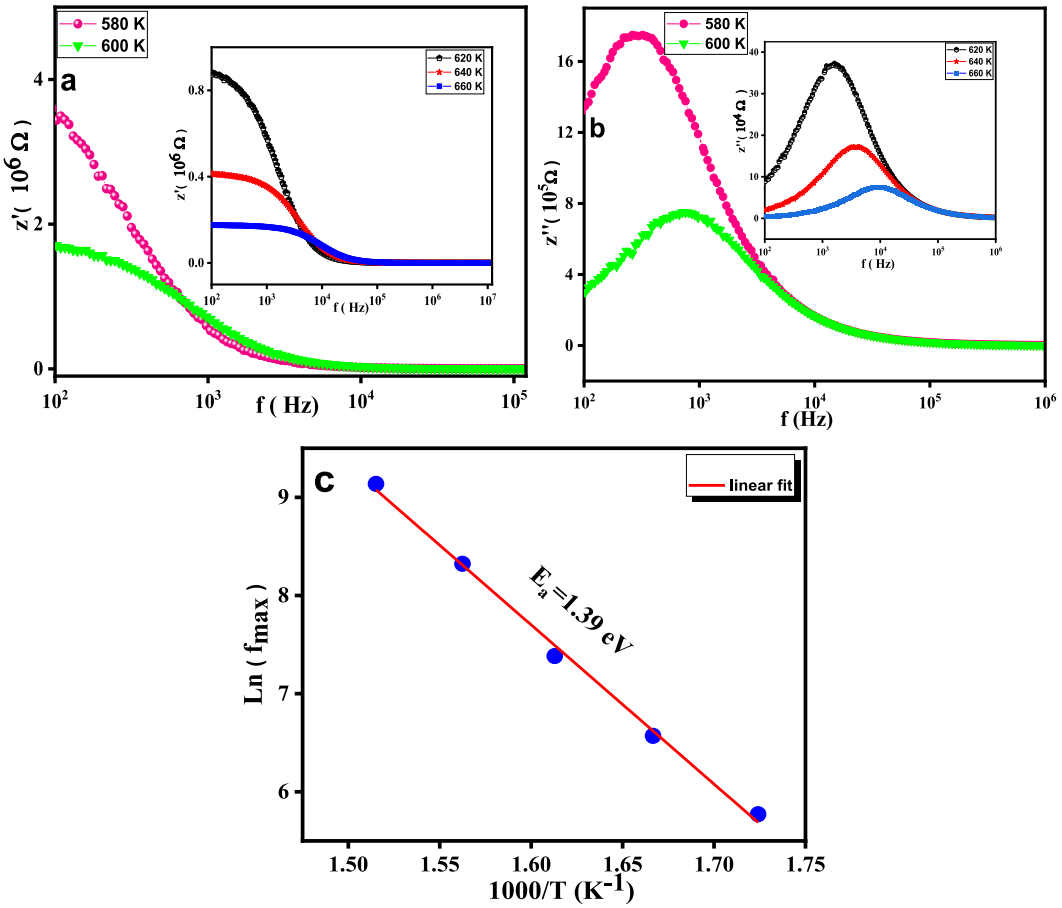

Fig. 3. The graphs labeled (a) and (b) depict the changes in Z′ and Z″ concerning frequency for BCTYO at different temperatures. Additionally, graph (c) illustrates the progression of Ln(fmax) concerning 1000/T for the BCTYO compound.

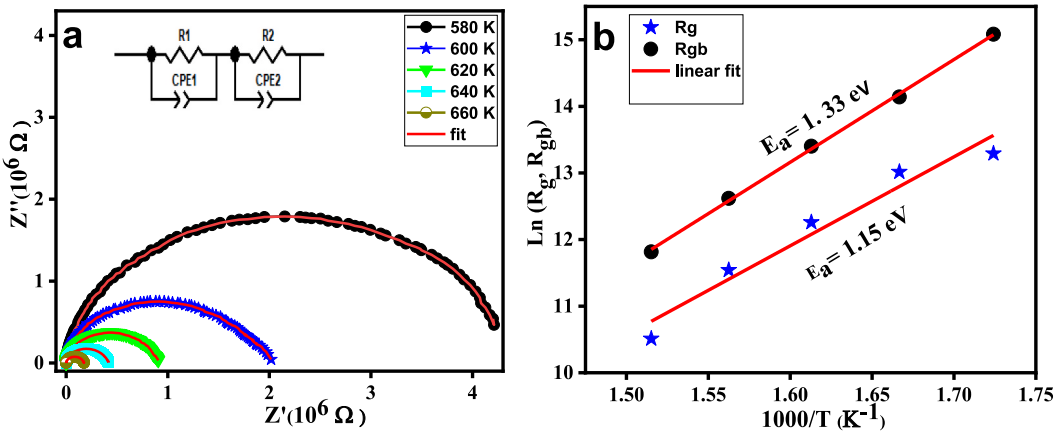

Fig. 4. (a) Nyquist diagrams of the compound BCTYO at various temperatures, along with the corresponding fit (red line). In (b), the plot illustrates the relationship between ln (R_g, Rgb) and 1000/T of the BCTYO. (For interpretation of the references to colour in this figure legend, the reader is referred to the Web version of this article.)

circuit determined using ZView Software [48] was exploited to explain the electrical behavior of the studied material. We used an equivalent electrical circuit that was composed of a combination of the two circuits Rg //CPEg and Rgb//CPEgb. Where Rg is the resistance of grain, R_{gb} is the resistance of grain boundary, and (CPE) is the constant phase element impedance to obtain the adjustment process. The aforementioned program provides the appropriate circuits that model the electrical responses of the material. Equations (5) and (6) give the calculation of Z′ and Z″ from the equivalent circuit.

$$z' = \frac{Rg}{(1 + Rg\omega\ CPEg)^2} + \frac{Rgb}{(1 + Rg\omega\ CPEg)^2} \tag{5}$$

$$z'' = \frac{-Rg^2\omega\ CPEg}{(1 + Rg\omega\ CPEg)^2} + \frac{-Rgb^2\omega\ CPEgb}{(1 + Rg\omega\ CPEg)^2} \tag{6}$$

The corresponding configuration is of type (Rg// CPEg) + (Rgb // CPEgb) [49] as shown in Fig. 4(a).
The Z_{CPE} impedance in general is described by equation (7) [49]:

$$Z_{CPE} = \frac{1}{Q(j\omega)^{\alpha}} \tag{7}$$

Where Q and α are the CPE parameters that are independent of frequency and ω is the angular frequency. The estimated Equivalent circuit parameters are collated in Table 2.

From the values found in Table 2, we notice that the grain boundary resistance Rgb is much higher than the grain boundary resistance Rg. Consequently, We can draw the conclusion that the material's conduction mechanism is caused by the grain boundaries [50]. In addition, we observe that the Rgb value decreases with increasing temperature, which is the result of the semiconducting nature of the material [51].

Two parallel lines are formed in the logarithmic representation of the evolution of the two resistances vs. 1000/T (Fig. 4(b)), demonstrating that Rgb and Rg are in accordance with the Arrhenius law as stated in equation (8) [52]:

$$R_{gb,g} = R_0 \exp\left(\frac{E_a}{k_B.T}\right) \tag{8}$$

With: KB is the Boltzmann constant, Ea is the activation energy, and R0 is a preexponential factor. The activation energy was determined to be 1.33 eV. This value is very similar to that determined from the relationship between Ln (fmax) and 1000/K. The high values of the activation energies are due to oxygen vacancies; this has already been observed in many perovskites [53,54]. In addition,

Table 2
Equivalent circuit parameters of the compound BCTYO.

T(K)	R_g (10^5 Ω)	CPE (10^{-10} F)	α_g	R_{gb} (10^5Ω)	CPE (10^{-10}F)	α_{gb}
580	5.916	2.573	0.983	35.49	1.926	**0.987**
600	4.496	1.771	0.989	13.852	2.426	**0.989**
62	2.108	1.717	0.992	6.605	2.296	**0.987**
640	1.028	1.61	0.995	3.020	2.255	**0.986**
660	0.367	1.65	1	1.352	1.885	**0.998**

the setting in motion of the oxygen vacancies that occurs with increasing temperature also contributes to this activation value; itself enhanced by the tendency for wall pinning that occurs due to excess oxygen vacancies at elevated temperatures.

The electric conductivity was calculated by exploiting the measurements made by impedance spectroscopy by the following relation (**9**):

$$\sigma = \frac{e}{s}\,\frac{Z'}{(Z'^2 + Z''^2)} \tag{9}$$

with, e and s present the thickness and the surface of the pellet, receptivity.

In Fig. 5(a), the graph illustrates the evolution of the conductivity vs. frequency at various temperatures. The graph shows two distinct behaviors. At low frequencies, the first behavior is shown as a plateau. This plateau denotes the compound's direct current conductivity ($\sigma = \sigma_{dc}$). The conductivity value remains relatively constant within a specific frequency range. However, this conductivity is influenced by temperature and exhibits changes as the temperature increases. Specifically, as the temperature rises, the value of σ_{dc} also increases. This suggests that the compound's conduction pathway is thermally activated, meaning that higher temperatures facilitate greater conductivity. The second behavior, observed beyond the plateau in the logarithmic scale, is characterized by a change in the slope of the σ_{AC} conductivity as a function of frequency. This suggests a different conduction mechanism or behavior compared to the plateau region. The exact nature of this change in slope would require further analysis or additional information in the context of the study or experiment.

Jonscher's law, also known as the universal power law or the power law model, is a popular explanation for the phenomenon of conductivity dispersion at elevated frequencies. It describes how the electrical conductivity of materials varies with frequency. In line with Jonscher's law, the complex electrical conductivity (σ*) of a material can be expressed by equation (10) [55]:

$$\sigma(\omega) = \sigma_{dc} + A\omega^{s} \tag{10}$$

ω: is the angular frequency; $\boldsymbol{\sigma_{dc}}$: the temperature-dependent low-frequency conductivity; **A**: the temperature-dependent coefficient; and s indicates the degree of interaction between mobile charge carriers and their surroundings [56].

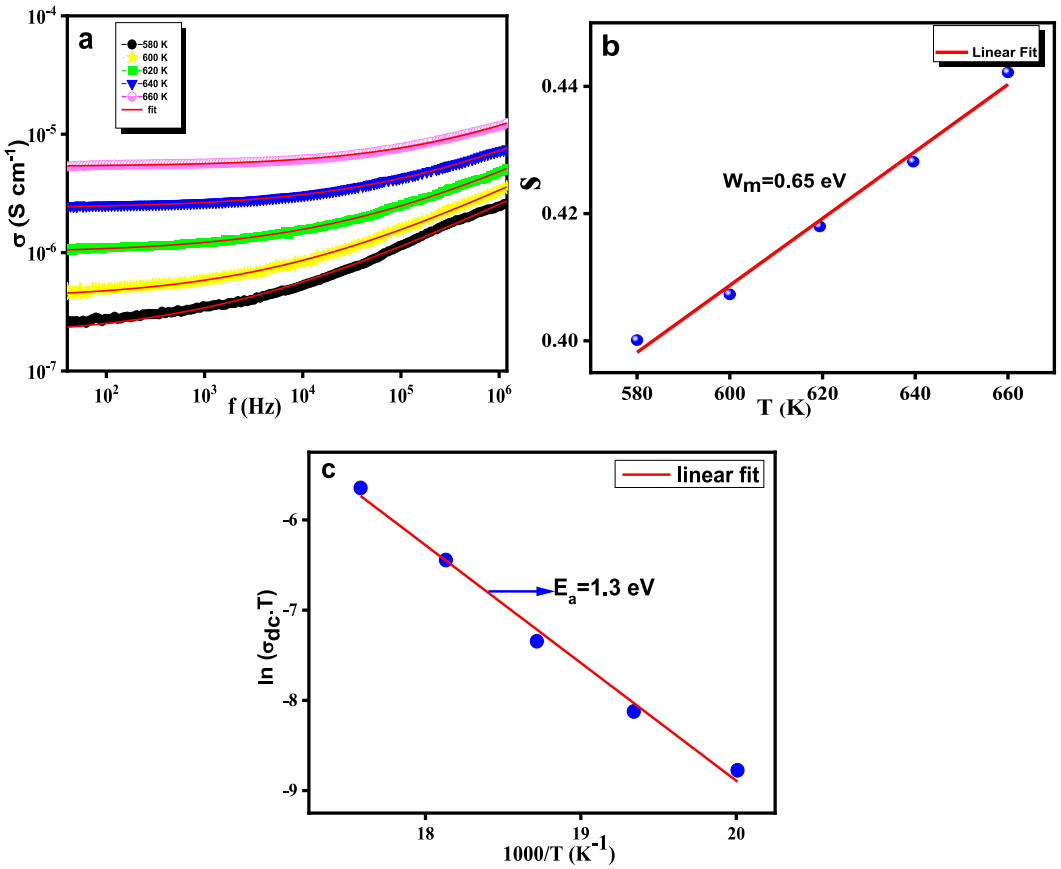

Fig. 5. (a) 5 illustrates the following how conductivity changes with frequency at various temperatures.; (b). How the exponent "s" varies concerning temperature; (c) The variation of $\ln(\sigma_{ac}T)$ as a function of 1000/T of the compound BCTYO.

To summarize, the study indicates a strong correlation between experimental and theoretical conductivity graphs when using Equation (10). Table 3 provides the parameter values of **'s'** at different temperatures. The square of the linear correlation coefficient, denoted as R^2, is commonly compared to one to assess the quality of the fit. Specifically, within the temperature range of 580–660 K, the values of the exponent 's' exhibit a consistent increase as the temperature rises. This observation implies the existence of a single conducting unit in the compound, which is associated with the Small Polaron Tunnel Model (NSPT) as indicated by Ref. [57].

Based on this model, the exponent "s" is given by the following formula [58]:

$$s = 1 + \frac{4k_bT}{W_m} \tag{11}$$

The binding energy of the Polaron is related to the maximum height of the barrier for infinite interstate separation, which is called the parameter W_m. According to Equation (11), we can estimate the W_m value by applying a linear fit in the variation of the "s" exponent vs. temperature (Fig. 5(b)), which equals 0.65 eV.

To estimate the $\mathbf{E_a}$ of the conduction process, we have plotted in Fig. 5(c) the variation of $\ln(\sigma_{ac}T)$ vs. 1000/T. As can be seen, the linear fit extends over the entire temperature range. As a result, the conduction mechanism may be inferred to follow the small polaron hopping (SPH) model established by Mott and Davis [59] (Equation (12)):

$$\sigma_{dc}.T = \sigma_0 e^{\frac{-E_a}{k_BT}} \tag{12}$$

We notice that the activation energy E_a calculated from $\ln(f_{max})$ vs. 1000/T, closely resembles the one obtained from the analysis of. This similarity suggests that the conduction process and the relaxation phenomenon share the same type of load carriers [60].

6. Dielectric properties as a function of temperature and frequency

Fig. 6(a) depicts the temperature dependence of εr′ at a wide range of frequencies for the BCTYO ceramic. The results clearly indicate a gradual increase in the dielectric constant as the temperature rises, reaching a maximum value of 16,706 at a temperature of 380 K. The inverse of permittivity (1/εr') at a frequency of 11 MHz displays a minimum point on the curve at 380 K, indicating the occurrence of the ferroelectric-to-paraelectric phase transition. This minimum point provides evidence of classical ferroelectric behavior, and the thermal dependence of 1/ εr' follows the Curie-Weiss type as stated in Equation (13) [61]:

$$\varepsilon r' = C/(T - T0) \tag{13}$$

where is the Curie constant and T0 Curie-Weiss temperature.

In Fig. 6 (b), the curve represents the variation of log (1/εr'-1/εr'max) as a function of log (T-Tc). The linear fit on this curve yields a value of γ=0.90, which is approximately equal to 1. This confirms the classical behavior mentioned above. Our material has been extensively examined and described due to its desirable characteristics and potential technological applications. It offers a wide range of useful properties, including high permittivity (used in capacitors), non-volatile memories, optical devices (2.5 eV), and electronic devices [62,63].

Based on the description provided, it seems like Fig. 7(a) is showing the change in electrical permittivity, represented as εr' with respect to frequency. The behavior of εr' reveals a slight decrease over the entire range of frequencies explored, then rapidly lowers with a higher frequency up to 10^5 Hz. Above this frequency value, the ε_r' spectra appear as superimposed plateaus. This material can be used for various applications, such as energy storage in electronic devices requiring high capacitance capacitors. Since this material has high ε_r' values (on the order of 10^3), it is therefore considered a good dielectric material. The high permittivity values can be attributed to various types of polarization and are mainly caused by the existence of (SCZ) [60,64]. Studies by S. MKhetrea [65] and S. Asad Ali [60] indicate that at high frequencies, the values of $\boldsymbol{\varepsilon_r'}$ decrease until they stabilize at a constant level. This behavior can be explained by the Maxwell - Wagner interfacial polarization, which arises when a dielectric material consists of two phases. The first phase is composed of conductive grains, and the second phase is constituted by the poorly conducting joints of these grains [64,66].

Understanding the origin of dielectric losses, electrical and dipolar ***dielectric*** losses, and electrical and dipolar relaxation times can all be supported by studying dielectric properties [67].

Fig. 7(b) depicts how **(εr'')** changes concerning frequency and temperature. To compute the permittivity, one can utilize the following equation (14).

$$\varepsilon'' = \frac{\sigma}{\omega\varepsilon_0} \tag{14}$$

Table 3
Results of the fitting parameters of the compound BCTYO.

T(K)	σ_{dc} (10^{-7}) $\Omega^{-1}cm^{-1}$	A (10^{-8})	S	R^2
580	1.93	0.93	0.400	0.9961
600	4.08	1.05	0.407	0.9992
620	9.96	1.30	0.417	0.9991
640	23.77	1.53	0.428	0.9992
660	53.43	1.35	0.442	0.9988

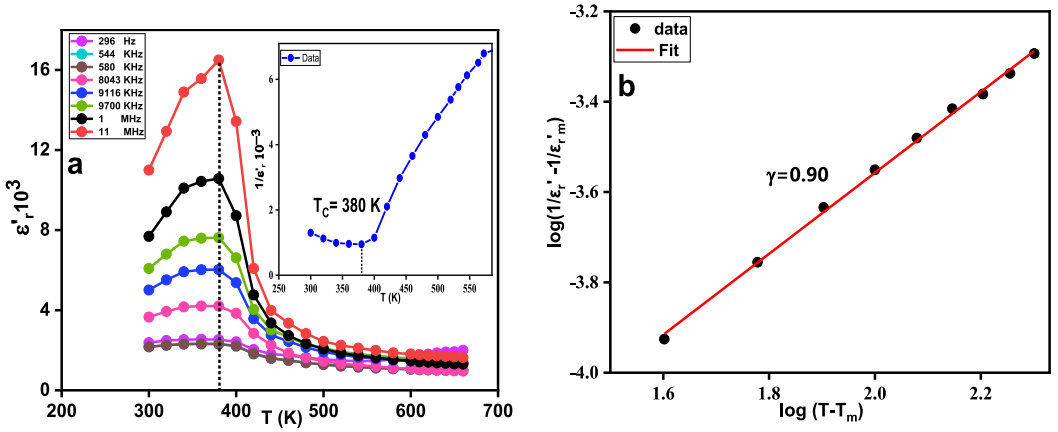

Fig. 6. (a), the real part of the relative permittivity (εr') is depicted as it varies with temperatures at different frequencies. (b) Illustrates the Variation of log (1/εr' - 1/ ε'_{rmax}) as a function of log(T-Tc) at high frequency.

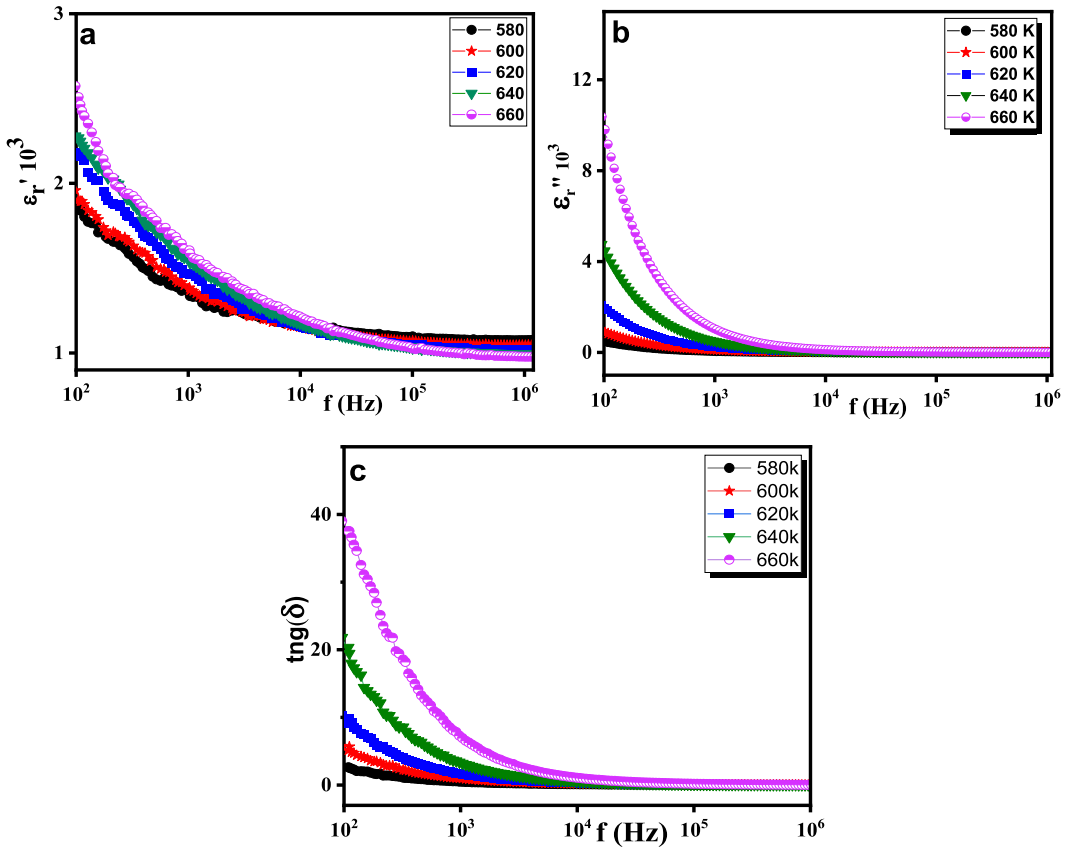

Fig. 7. (a; b; c) show respectively the Variation of the real component (εr'); t imaginary part (εr''), and loss factor tan(δ) concerning frequency and temperature.

With: σ: the conductivity, ω = 2πf: the angular frequency and ε_0 = permittivity of vacuum is equal to 8.854 × 10^{-12} F/m.

We notice that ε_r'' is quite high at elevated temperatures and low frequencies. The reason behind the gathering of charges at the electrode-compound junction is clarified by the presence of ion diffusion effects, particularly when the material's characteristics do not adhere to the Debye model [68]. It is well-known that electrical energy loss is essentially linked to conduction, dielectric resonance, and dielectric relaxation, which can be estimated using a material's tan(δ) values [69]. ε' and ε'' as are linked between them by the

following relationship (15) [70]:

$$tng\ (\delta) = \frac{\varepsilon''}{\varepsilon'} \tag{15}$$

tan(δ) is relatively high for low temperatures and frequencies, and they become very low when the frequency increases, regardless of the temperature value (Fig. 7(c)).

The complex modulus formalism can also be used to examine the experimental results. This method provides an alternate viewpoint on electrical characteristics and solves issues such as electrode polarization [71,72]. The real and imaginary components of the modulus M*(ω) were computed from the permittivity ε*(ω) using Equation (16):

$$M' = \frac{\varepsilon'}{\varepsilon'^2 + \varepsilon''^2} = \omega C_0 Z'' \quad \text{et} \quad M'' = \frac{\varepsilon''}{\varepsilon'^2 + \varepsilon''^2} = \omega C_0 Z' \tag{16}$$

Fig. 8(a) demonstrates that M′ exhibits minimal values at low frequencies when observed at different temperatures.

This result demonstrates that the electrode effects are insignificant and can be ignored [73]. At high frequencies, however, the value of M′ keeps rising as the frequency increases until it stabilizes at a constant value identical to M_∞ ($M_\infty = 1/\varepsilon_\infty$). This phenomenon can be attributed to relaxation processes.

Fig. 8(b) shows the variation (M″) vs. frequency at different temperatures. With increasing temperature, the positions of the peaks shift towards higher frequencies, suggesting that the relaxation time lengthens as a result of the thermal activation of charge carriers. As a result, the highest peaks move to higher frequencies as the temperature rises. The frequency range centered on fmax is rather limited and represents the shift from short-range to long-range charge carrier mobility, especially for decreasing frequencies. Frequencies below fmax reflect long-range charge carrier movements, whereas frequencies above fmax depict carriers that are more constrained in their potential wells.

7. Thermoelectric properties

Barium oxide titanate is considered a suitable material for thermoelectric applications [74]. The thermoelectrical properties were examined using the BoltzTraP code and presented in Fig. 9.

The ZT scale of merit $ZT = \frac{\sigma S^2 T}{k}$ is used to quantify the thermoelectric effectiveness. Where the electrical conductivity, thermal conductivity, Seebeck coefficient, and temperature, are represented by σ, k and, T, respectively. Those parameters were calculated, according to the classical Boltzmann transport theory using the following relations (17, 18, 19) [23,75]:

$$\sigma_{\alpha\beta}(T,\mu) = \frac{1}{e T \Omega} \int \sigma_{\alpha\beta}(\varepsilon)(\varepsilon - \mu)\left[-\frac{\partial f_\mu(T,\varepsilon)}{\partial \varepsilon}\right] d\varepsilon \tag{17}$$

$$k^0_{\alpha\beta}(T,\mu) = \frac{1}{e T \Omega} \int \sigma_{\alpha\beta}(\varepsilon)(\varepsilon - \mu)^2\left[-\frac{\partial f_\mu(T,\varepsilon)}{\partial \varepsilon}\right] d\varepsilon \tag{18}$$

$$S_{\alpha\beta}(T,\mu) = \sigma_{\alpha\beta}(T,\mu)^{-1} \vartheta_{\alpha\beta}(T,\mu) \tag{19}$$

At a temperature of 300 K, we observed that the electrical conductivity (σ/τ) reached a value of 5 × 10^18 Ω^{-1} m^{-1} (Fig. 9-a). Fig. 9-b shows a steady rise in thermal conductivity (k) with temperature, showing the sample's behavior as a semiconductor. Fig. 9(c) shows that the hole contribution dominates the electric conduction by having positive S values [76]. Furthermore, significant values of

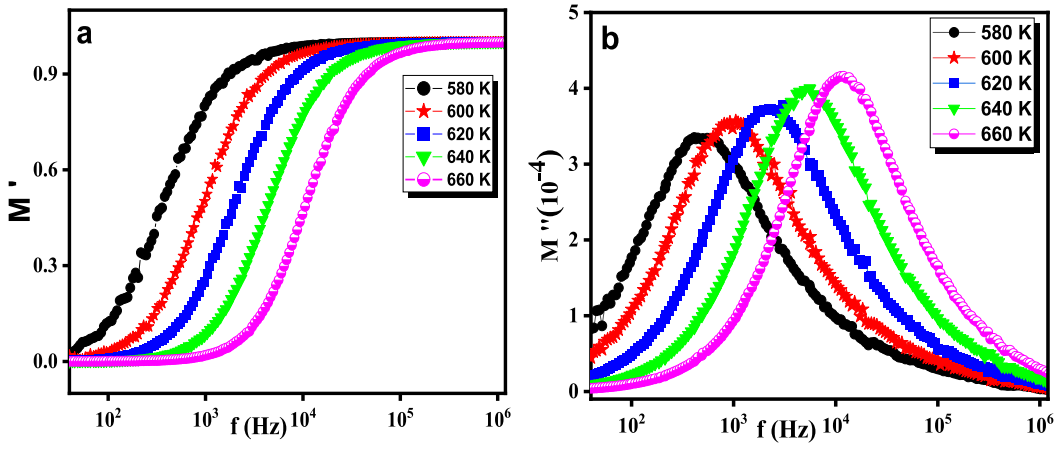

Fig. 8. (a; b) Variation (M′) and *(M″) of the complex modulus* (M*(ω)) vs. frequency at different temperatures.

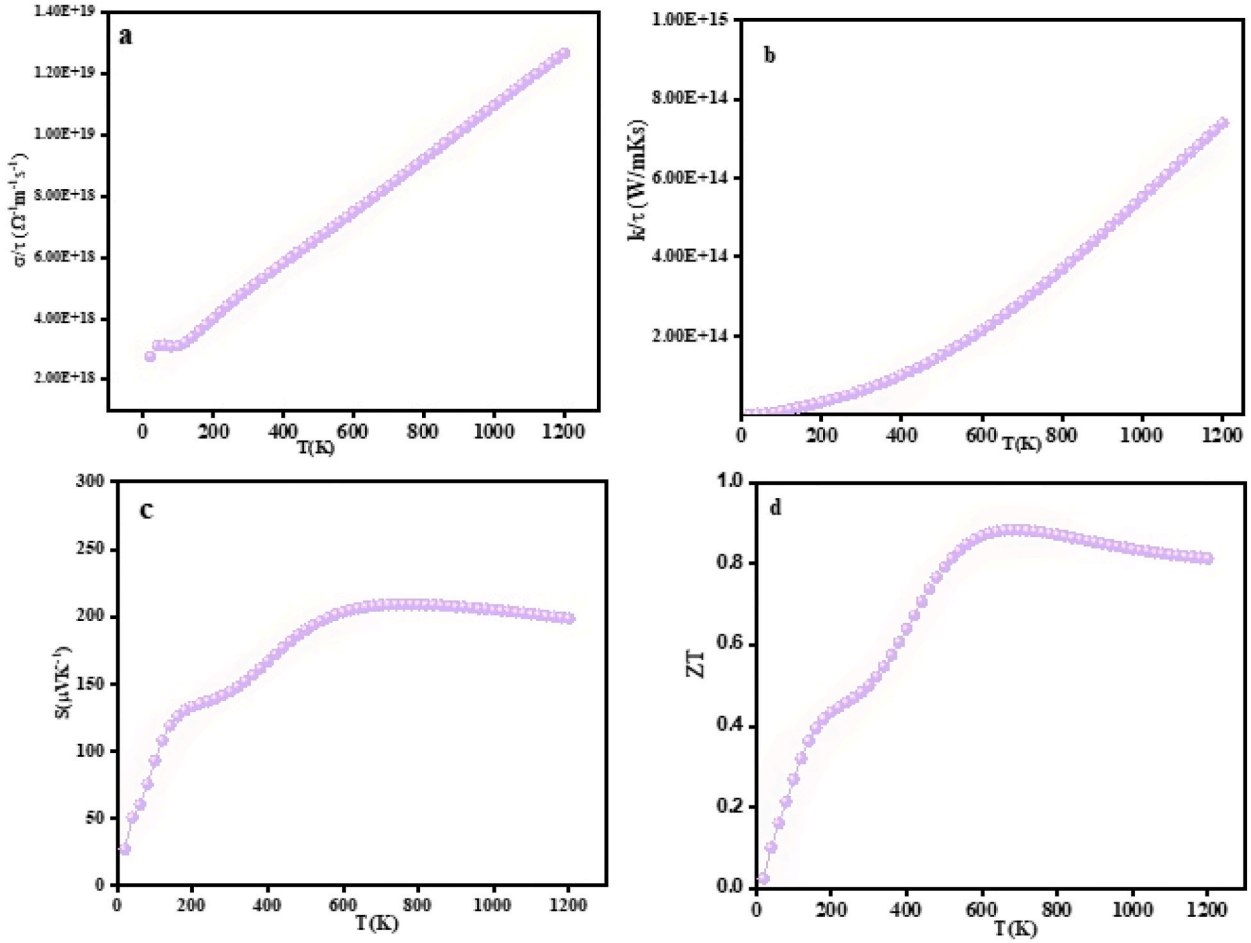

Fig. 9. (a) shows Electrical conductivity, (b) thermal conductivity, (c) Seebek coefficient and d) ZT merit factor.

S were observed, reaching 140 μV K^{-1} at 300 K and increasing to 210 μV K^{-1} at 600 K. In order to evaluate the performance of $Ba_{0.95}Ca_{0.05}Ti_{0.95}Y_{0.05}O_{2.975}$ in thermoelectric (TE) applications, the evolution of the merit factor ZT with temperature is depicted in Fig. 9-d. It was observed that ZT increases with rising temperature, primarily due to the enhancement of the S coefficient. The ZT value reached an intriguing value of 0.9 in the neighborhood of 600 K, showing its potential as a good option for high-temperature thermoelectric devices.

8. Conclusion

In the mentioned study, co-doping of $BaTiO_3$ ceramics with Ca^{2+} and Y^{3+} was explored through computational simulations utilizing Density Functional Theory (DFT) and first-principles calculations. This computational approach allows to predict and analyze various properties of the material, including optical and electronic properties. The structural analysis of $Ba_{0.95}Ca_{0.05}Ti_{0.95}Y_{0.05}O_{2.975}$ was performed by employing X-ray diffraction, it showed that the compound forms a tetragonal structure characterized by the *P*4*mm* space group. The electronic characteristics of BCTYO were investigated using the TB-mBJ calculation approximation, which revealed an indirect gap reached 2.5 eV. Impedance spectra of the BCTYO compound were distinguished by the presence of temperature-dependent semi-circular arcs. The investigation of the real component of the permittivity as a function of temperature revealed a phase transition from the FE to the PE phase at Tc = 380 K. Our material has a wide range of uses and does not have any negative impact on the environment. Furthermore, the examination of the thermoelectric characteristics proves a favorable merit factor ZT at 600 which reaches 0.9. This intriguing outcome leads us to contemplate BCTYO as a potential and promising option for application in thermoelectric devices.

Author contribution statement

A. Saidi: Wrote the paper, Analyzed and interpreted the data. A. Mabrouki; E. Dhahri: Analyzed and interpreted the data. R. Dhahri: Contributed reagents, materials, analysis tools or data. B. Costa: Performed the experiments. Khirouni: Conceived and designed the

experiments. Data availability statement: Data will be made available on request.

Declaration of interest's statement

The authors declare that they have no known competing financial interests or personal relationships that could have appeared to influence the work reported in this paper.

Declaration of competing interest

The authors declare that they have no known competing financial interests or personal relationships that could have appeared to influence the work reported in this paper.

References

[1] A. Mabrouki, A. Benali, T. Mnasri, E. Dhahri, M.A. Valente, M. Jemmali, Oxygen deficiency effect on the magnetocaloric and critical phenomena for La0.8□0.2MnO3-Δ (Δ = 0, 0.1 and 0.2) compounds: significant enhancement of relative cooling power, J. Mater. Sci. Mater. Electron. 31 (2020) 22749–22767.
[2] O. Messaoudi, A. Mabrouki, M. Moufida, L. Alfhaid, A. Azhary, S. Elgharbi, Correlation between experimental and DFT calculations of photocatalytic and optical properties of La0.8Nd0.1Sr0.1MnO3 perovskite: degradation efficiency of methyl orange dye under visible-irradiated conditions, J. Mater. Sci. Mater. Electron. 32 (2021) 22481–22492.
[3] A. Mabrouki, H. Chadha, O. Messaoudi, A. Benali, T. Mnasri, E. Dhahri, M.A. Valente, S. Elgharbi, Ah Dhahri, L. Manai, Experimental and theoretical study of magnetic and magnetocaloric properties of the lacunar La0.8□0.2MnO2.8 compound: bean-Rodbell model, Inorg. Chem. Commun. 139 (2022), 109310.
[4] I. Dhahri, A. Mabrouki, M. Ellouze, E. Dhahri, S. Labidi, E.K. Hlil, R. Masrour, Simulation study by phenomenological and Bean–Rodbell methods of La0.7Sr0.3Mn0.95Fe0.05O3 compound, Indian J. Phys. 96 (2022) 3509–3515.
[5] H. Abdelkefi, H. Khemakhem, A. Simon, J. Darriet, X-ray diffraction study of Ba0.985Na0.015Ti0.985Nb0.015O3, Ba0.6Na0.4Ti0.6Nb0.4O3 and Ba0.3Na0.7Ti0.3Nb0.7O3 compositions, J. Alloys Compd. 463 (2008) 423–427.
[6] Z.G. Hu, Y.W. Li, M. Zhu, Z.Q. Zhu, J.H. Chu, Microstructural and optical investigations of sol–gel derived ferroelectric BaTiO3 nanocrystalline films determined by spectroscopic ellipsometry, Phys. Lett. 372 (2008) 4521–4526.
[7] J. Xu, J. Zhai, X. Yao, Structure and dielectric nonlinear characteristics of BaTiO3 thin films prepared by low temperature process, J. Alloys Compd. 467 (2009) 567–571.
[8] F. Wan, J. Han, Z. Zhu, Dielectric response in ferroelectric BaTiO3, Phys. Lett. 372 (2008) 2137–2140.
[9] A. Krause, W.M. Weber, D. Pohl, B. Rellinghaus, A. Kersch, T. Mikolajick, Investigation of band gap and permittivity of the perovskite CaTiO3 in ultrathin layers, J. Phys. Appl. Phys. 48 (2015), 415304.
[10] N. Baskaran, H. Chang, Thermo-Raman and dielectric constant studies of CaxBa1- xTiO3 ceramics, Mater. Chem. Phys. 77 (2003) 889–894.
[11] F.A. Ismail, R.A.M. Osman, M.S. Idris, Review on dielectric properties of rare earth doped barium titanate, in: AIP Conference Proceedings, AIP Publishing LLC, 2016, 090005.
[12] E. Palaimiene, J. Macutkevic, J. Banys, A. Winiarski, I. Gruszka, J. Koperski, A. Molak, Crossover from ferroelectric to relaxor behavior in Ba1- x Ca x TiO3 (x= 0.17) system, Materials 13 (2020) 2854.
[13] J.-Y. Chen, Y.-W. Tseng, C.-L. Huang, Improved high Q value of (1- x) Ca (Mg1/3Ta2/3) O3–xCa0. 8Sm0. 4/3TiO3 solid solution with zero temperature coefficient of resonant frequency, J. Alloys Compd. 494 (2010) 205–209.
[14] L.M. Garten, M. Burch, A.S. Gupta, R. Haislmaier, V. Gopalan, E.C. Dickey, S. Trolier-McKinstry, Relaxor ferroelectric behavior in barium strontium titanate, J. Am. Ceram. Soc. 99 (2016) 1645–1650.
[15] M. Shandilya, R. Rai, A. Zeb, S. Kumar, Modification of structural and electrical properties of Ca element on barium titanate nano-material synthesized by hydrothermal method, Ferroelectrics 520 (2017) 93–109.
[16] S. Bernhardt, H. Veenhuis, P. Delaye, R. Pankrath, G. Roosen, Effect of rhodium doping on the photorefractive properties of BCT crystals at 850 nm, Appl. Phys. B 72 (2001) 667–675.
[17] H. Trabelsi, M. Bejar, E. Dhahri, M. Sajieddine, K. Khirouni, P.R. Prezas, B.M.G. Melo, M.A. Valente, M.P.F. Graca, Effect of oxygen vacancies on SrTiO3 electrical properties, J. Alloys Compd. 100 (2017) 894–903.
[18] M. Tihtih, J.E.F. Ibrahim, M.A. Basyooni, R. En-Nadir, W. Belaid, I. Hussainova, I. Kocserha, Development of yttrium-doped BaTiO3 for next-generation multilayer ceramic capacitors, ACS Omega 8 (2023) 8448–8460.
[19] I. Mahariq, H. Kurt, On-and off-optical-resonance dynamics of dielectric microcylinders under plane wave illumination, JOSA B 32 (2015) 1022–1030.
[20] I. Mahariq, M. Kuzuoglu, I.H. Tarman, H. Kurt, Photonic nanojet analysis by spectral element method, IEEE Photon. J. 6 (2014) 1–14.
[21] I. Mahariq, On the application of the spectral element method in electromagnetic problems involving domain decomposition, Turk. J. Electr. Eng. Comput. Sci. 25 (2017) 1059–1069.
[22] I. Mahariq, V.N. Astratov, H. Kurt, Persistence of photonic nanojet formation under the deformation of circular boundary, JOSA B 33 (2016) 535–542.
[23] O. Messaoudi, A.E. Mabrouki, L. Alfhaid, L. Manai, A. Azhary, Effect of annealing temperature on the photocatalytic activity of La0.8Nd0.1Sr0.1MnO3 manganite for methyl orange degradation and study of its thermoelectric properties using DFT calculations, J. Mater. Sci. Mater. Electron. 34 (2023) 827.
[24] A. Mabrouki, A. Bougoffa, A. Trabelsi, E. Dhahri, K. Khirouni, Optical and thermoelectric properties of NaNbO3 thin film deposed by spray pyrolysis: experimental and DFT study, Eur. Phys. J. Plus. 137 (2022) 748.
[25] W. Zhang, K. Zhu, J. Liu, J. Wang, K. Yan, P. Liu, Y. Wang, Influence of the phase transformation in NaxCoO2 ceramics on thermoelectric properties, Ceram. Int. 44 (2018) 17251–17257.
[26] F. Delorme, P. Diaz-Chao, E. Guilmeau, F. Giovannelli, Thermoelectric properties of Ca3Co4O9–Co3O4 composites, Ceram. Int. 41 (2015) 10038–10043.
[27] B. Feng, X. Jiang, Z. Pan, L. Hu, X. Hu, P. Liu, Y. Ren, G. Li, Y. Li, X. Fan, Preparation, Structure, and enhanced thermoelectric properties of Sm-doped BiCuSeO oxyselenide, Mater. Des. 185 (2020).
[28] C. Chen, M.A. Bousnina, F. Giovannelli, F. Delorme, Influence of Bi on the thermoelectric properties of SrTiO3-δ, J. Materiomics 5 (2019) 88–93.
[29] L. Han, N. Van Nong, W. Zhang, T. Holgate, K. Tashiro, M. Ohtaki, N. Pryds, S. Linderoth, Effects of morphology on the thermoelectric properties of Al-doped ZnO, RSC Adv. 4 (2014) 12353–12361.
[30] T. Maiti, M. Saxena, P. Roy, Double perovskite (Sr2B′ B ″O6) oxides for high-temperature thermoelectric power generation—a review, J. Mater. Res. 34 (2019) 107–125.
[31] H.M. Rietveld, A profile refinement method for nuclear and magnetic structures, J. Appl. Crystallogr. 2 (1969) 65–71.
[32] Y. Marouani, A. Mabrouki, R. Dhahri, E. Dhahri, B.F.O. Costa, Experimental and theoretical studies of structural, magnetic and electronic properties of Ba1-xSrxFe12O19 (x = 0, 0.5, 1) hexaferrites, Inorg. Chem. Commun. 136 (2022), 109163.
[33] A. Mabrouki, O. Messaoudi, M. Mansouri, S. Elgharbi, A. Bardaoui, Study of the structural, electronic, magnetic and magnetocaloric properties of La0.5Ca0.5Mn0.9V0.1O3 sample: first-principles calculation (DFT–MFT), RSC Adv. 11 (2021) 37896–37903.
[34] K. Schwarz, P. Blaha, G.K. Madsen, Electronic structure calculations of solids using the WIEN2k package for material sciences, Comput. Phys. Commun. 147 (2002) 71–76.

[35] L. Motevalizadeh, Z. Heidary, M.E. Abrishami, Facile template-free hydrothermal synthesis and microstrain measurement of ZnO nanorods, Bull. Mater. Sci. 37 (2014) 397–405.
[36] S. Hcini, S. Zemni, A. Triki, H. Rahmouni, M. Boudard, Size mismatch, grain boundary and bandwidth effects on structural, magnetic and electrical properties of Pr0. 67Ba0. 33MnO3 and Pr0. 67Sr0. 33MnO3 perovskites, J. Alloys Compd. 509 (2011) 1394–1400.
[37] Phys. Rev. Materials 7 (2023), 014202. - Single pair of type-III Weyl points half-metals: ${\text{BaNiIO}}_{6}$ as an example, (n.d.), https://journals.aps.org/prmaterials/abstract/10.1103/PhysRevMaterials.7.014202. accessed April 14, 2023.
[38] D.G. Ferschweiler, R. Blair, A.R. Klotz, Percolation and dissolution of Borromean networks, Phys. Rev. E. 107 (2023), 024304.
[39] C. Xie, H. Yuan, Y. Liu, X. Wang, Two-nodal surface phonons in solid-state materials, Phys. Rev. B 105 (2022), 054307.
[40] J. Wang, H. Yuan, Y. Liu, X. Wang, G. Zhang, Multiple dimensions of spin-gapless semiconducting states in tetragonal ${\mathrm{Sr}}_{2}{\mathrm{CuF}}_{6, Phys. Rev. B 106 (2022) L060407.
[41] S.H. Wemple, M. Didomenico Jr., I. Camlibel, Dielectric and optical properties of melt-grown BaTiO3, J. Phys. Chem. Solid. 29 (1968) 1797–1803.
[42] A. Mabrouki, T. Mnasri, A. Bougoffa, A. Benali, E. Dhahri, M.A. Valente, Experimental study and DFT calculation of the oxygen deficiency effects on structural, magnetic and optical properties of La0.8□0.2MnO3-δ (δ = 0, 0.1 and 0.2) compounds, J. Alloys Compd. 860 (2021), 157922.
[43] O. Polat, M. Caglar, F.M. Coskun, D. Sobola, M. Konecny, M. Coskun, Y. Caglar, A. Turut, Examination of optical properties of YbFeO3 films via doping transition element osmium, Opt. Mater. 105 (2020), 109911.
[44] J. Suchanicz, The low-frequency dielectric relaxation Na0. 5Bi0. 5TiO3 ceramics, Mater. Sci. Eng. B 55 (1998) 114–118.
[45] H. Rahmouni, B. Cherif, M. Smari, E. Dhahri, N. Moutia, K. Khirouni, Effect of exceeding the concentration limit of solubility of silver in perovskites on the dielectric and electric properties of half doped lanthanum–calcium manganite, Phys. B Condens. Matter 473 (2015) 1–6.
[46] A.I. Ali, C.W. Ahn, Y.S. Kim, Enhancement of piezoelectric and ferroelectric properties of BaTiO3 ceramics by aluminum doping, Ceram. Int. 39 (2013) 6623–6629.
[47] A. Dutta, C. Bharti, T.P. Sinha, Dielectric relaxation in Sr (Mg1/3Nb2/3) O3, Phys. B Condens. Matter 403 (2008) 3389–3393.
[48] D. Johnson, ZView: a Software Program for IES Analysis. Version 2.8. Southern Pines, Scribner Associates, NC, 2008.
[49] P. Zoltowski, On the electrical capacitance of interfaces exhibiting constant phase element behaviour, J. Electroanal. Chem. 443 (1998) 149–154.
[50] Y. Moualhi, R. Mnassri, M.M. Nofal, H. Rahmouni, A. Selmi, M. Gassoumi, N. Chniba-Boudjada, K. Khirouni, A. Cheikhrouhou, Magnetic properties and impedance spectroscopic analysis in Pr0. 7Ca0. 3Mn0. 95Fe0. 05O3 perovskite ceramic, J. Mater. Sci. Mater. Electron. 31 (2020) 21046–21058.
[51] S. Hcini, M. Hsini, H. Al Robei, M.L. Bouazizi, M. Boudard, Structural analysis and theoretical investigations of the magnetocaloric effect for La0. 7Ba0. 15Ag0. 15MnO3 manganite prepared using sol-gel route, J. Supercond. Nov. Magnetism 33 (2020) 3597–3605.
[52] M. Amghar, A. Bougoffa, A. Trabelsi, A. Oueslati, E. Dhahri, Structural, morphological, and electrical properties of silver-substituted ZnAl 2 O 4 nanoparticles, RSC Adv. 12 (2022) 15848–15860.
[53] B.K. Barick, K.K. Mishra, A.K. Arora, R.N.P. Choudhary, D.K. Pradhan, Impedance and Raman spectroscopic studies of (Na0. 5Bi0. 5) TiO3, J. Phys. Appl. Phys. 44 (2011), 355402.
[54] O. Raymond, R. Font, N. Suarez-Almodovar, J. Portelles, J.M. Siqueiros, Frequency-temperature response of ferroelectromagnetic Pb (Fe 1/ 2 Nb 1/ 2) O 3 ceramics obtained by different precursors. Part I. Structural and thermo-electrical characterization, J. Appl. Phys. 97 (2005), 084107.
[55] A.K. Jonscher, The 'universal'dielectric response, Nature 267 (1977) 673–679.
[56] K. Funke, Jump relaxation in solid electrolytes, Prog. Solid State Chem. 22 (1993) 111–195.
[57] S. Nasri, M. Megdiche, M. Gargouri, DC conductivity and study of AC electrical conduction mechanisms by non-overlapping small polaron tunneling model in LiFeP2O7 ceramic, Ceram. Int. 42 (2016) 943–951.
[58] F.B. Abdallah, A. Benali, S. Azizi, M. Triki, E. Dhahri, M.P.F. Graca, M.A. Valente, Strontium-substituted La0. 75Ba0. 25- xSrxFeO3 (x= 0.05, 0.10 and 0.15) perovskite: dielectric and electrical studies, J. Mater. Sci. Mater. Electron. 30 (2019) 8457–8470.
[59] N.F. Mott, Conduction in glasses containing transition metal ions, J. Non-Cryst. Solids 1 (1968) 1–17.
[60] H. Rahmouni, M. Nouiri, R. Jemai, N. Kallel, F. Rzigua, A. Selmi, K. Khirouni, S. Alaya, Electrical conductivity and complex impedance analysis of 20% Ti-doped La0. 7Sr0. 3MnO3 perovskite, J. Magn. Magn Mater. 316 (2007) 23–28.
[61] S. Mahajan, O.P. Thakur, C. Prakash, K. Sreenivas, Effect of Zr on dielectric, ferroelectric and impedance properties of BaTiO3 ceramic, Bull. Mater. Sci. 34 (2011) 1483–1489.
[62] N. Boutal, Nouveaux matériaux de type pérovskite simples ou complexes sans plomb, PhD Thesis, Faculté de Chimie, 2017.
[63] S. Satha, Elaboration et caractérisation des céramiques poreuses à base de BaTiO3, 2020.
[64] S. Ayachi, Y. Moualhi, H. Rahmouni, M. Gassoumi, K. Khirouni, Chromium concentration effects on transport and dielectric behavior of lanthanum-gallium ferrite, Phys. B Condens. Matter 591 (2020), 412244.
[65] S.M. Khetre, H.V. Jadhav, P.N. Jagadale, S.R. Kulal, S.R. Bamane, Studies on electrical and dielectric properties of LaFeO3, Adv. Appl. Sci. Res. 2 (2011) 503–511.
[66] A. Omri, M. Bejar, E. Dhahri, M. Es-Souni, M.A. Valente, M.P.F. Graca, L.C. Costa, Electrical conductivity and dielectric analysis of La0. 75 (Ca, Sr) 0.25 Mn0. 85Ga0. 15O3 perovskite compound, J. Alloys Compd. 536 (2012) 173–178.
[67] A. Omri, E. Dhahri, B.F.O. Costa, M.A. Valente, Study of structural, morphological, Mössbauer and dielectric properties of NiFeCoO4 prepared by a sol gel method, J. Sol. Gel Sci. Technol. 98 (2021) 364–375.
[68] B.V.R. Chowdari, R. Gopalakrishnan, AC conductivity analysis of glassy silver iodomolybdate system, Solid State Ionics 23 (1987) 225–233.
[69] L. Alexander, H.P. Klug, Determination of crystallite size with the X-Ray spectrometer, J. Appl. Phys. 21 (1950) 137–142.
[70] M. Amghar, A. Bougoffa, A. Trabelsi, A. Oueslati, E. Dhahri, Optical and dielectric properties of silver-substituted ZnAl 2 O 4 spinels synthesized using a sol-gel auto-combustion method, RSC Adv. 12 (2022) 20348–20359.
[71] M. Ganguli, M.H. Bhat, K.J. Raol, Lithium ion transport in Li2SO4–Li2O–B2O3 glasses, Phys. Chem. Glasses 40 (1999) 297–304.
[72] A. Saidi, A. Mabrouki, J. Dhahri, E. Dhahri, K. Khirouni, B.F.O. Costa, Effect of frequency on the classical and relaxor ferroelectric behavior of substituted titanate Ba 0.7 Er 0.16 Ca 0.05 Ti 0.91 Sn 0.09 O 3, Phys. Chem. Chem. Phys. 25 (2023) 17999–18010.
[73] N.H. Vasoya, P.K. Jha, K.G. Saija, S.N. Dolia, K.B. Zankat, K.B. Modi, Electric modulus, scaling and modeling of dielectric properties for Mn2+-Si4+ Co-substituted Mn-Zn ferrites, J. Electron. Mater. 45 (2016) 917–927.
[74] M. Ziati, H. Ez-Zahraouy, Theoretical investigation of electronic, optical and thermoelectric properties of tellurium doped barium titanate (BTO) through modified Becke – johnson exchange potential, Optik 231 (2021), 166440.
[75] O. Sahnoun, H. Bouhani-Benziane, M. Sahnoun, M. Driz, Magnetic and thermoelectric properties of ordered double perovskite Ba2FeMoO6, J. Alloys Compd. 714 (2017) 704–708.
[76] J. Liu, Q.-Y. Jiang, S.-D. Zhang, H. Zhang, Carrier mobility and relaxation time in BiCuSeO, Phys. Lett. 383 (2019), 125990.